

Agentic Additive Manufacturing Alloy Discovery

Peter Pak,[†] Achuth Chandrasekhar,[†] and Amir Barati Farimani^{*,†,‡}

[†] *Department of Mechanical Engineering, Carnegie Mellon University, Pittsburgh, PA, USA*

[‡] *Machine Learning Department, Carnegie Mellon University, Pittsburgh, PA, USA*

E-mail: barati@cmu.edu

Abstract

Agentic systems enable the intelligent use of research tooling, augmenting a researcher’s ability to investigate and propose novel solutions to existing problems. Within Additive Manufacturing (AM), alloy discovery remains a complex challenge, often requiring expertise in the various domains of materials science, thermodynamic simulations, and experimental analysis. Large Language Model (LLM) enabled agents can facilitate this endeavor by utilizing their extensive knowledge base to dispatch tool calls via Model Context Protocol (MCP) to perform actions such as Thermo-Calc property diagram calculations and lack of fusion process map generation. In addition, the multi-agent system developed in this work is able to effectively reason through complex user prompts and provide analysis on the printability of proposed alloys. These agents can dynamically adjust their task trajectory to the outcomes of tool call results, effectively enabling autonomous decision-making in practical environments. This work aims to utilize LLM enabled agents to automate and accelerate the task of alloy discovery within the field of additive manufacturing and showcase the benefits of adopting this multi-agent system.

1 Introduction

The discovery of new alloys remains a pressing need in Additive Manufacturing (AM) particularly in industries involved in biomedical, aerospace, or energy applications.¹⁻⁶ Specifically, considerations such as deformation,⁷⁻⁹ corrosion resistance,^{1,10} and biocompatibility¹¹⁻¹³ continue to be key motivators for novel alloy development. However, the discovery and validation of new AM alloys remains a time-consuming process often requiring expertise in materials science, computational simulations, and experimental analysis.^{2,4,5} Furthermore, each alloy has a unique set of build parameters that are necessary to avoid potential defects within part fabrication that are often determined from simulation analysis and / or experimental trials.

For the task of alloy discovery, Computer Calculation of Phase Diagrams¹⁴ (CALPHAD) is commonly performed to calculate the individual phases of an alloy via Gibbs Free Energy and numerical optimization. CALPHAD provides a rigorous thermodynamic framework for predicting equilibrium phase stability and composition in multicomponent alloys by combining assessed Gibbs energy descriptions of individual phases with numerical minimization of the total free energy. In practice, modern CALPHAD workflows go beyond phase fields: well-curated mobility and property databases enable prediction of temperature-dependent thermophysical quantities (eg., k , C_p , ρ).^{15,16} Thermo-Calc¹⁷ provides a software suite to perform this task with a library of resources to obtain relevant information regarding the various elements, alloys, and application properties.

With the procurement of the material properties of an AM alloy candidate, insight into the alloy's printability is assessed through numerical solvers. Solvers such as those developed by Eagar-Tsai¹⁸ and Rosenthal¹⁹ provide fast insight into the temperature field of a melt pool through an analytical solution. Whereas, solvers such as OpenFOAM²⁰ and FLOW-3D²¹ utilize Computational Fluid Dynamics (CFD) provide more detailed analysis of the underlying fluid flow, heat transfer, and solidification phenomena of the melt pool.^{22,23}

The development of Agentic Tools have enabled the use of Large Language Models (LLMs) to achieve complex tasks beyond the context of the prompt window. Examples of

this include the monitoring and adjustment of real-time Fused Deposition Modeling (FDM) builds,²⁴ search and discovery of potential catalyst and drug candidates,^{25,26} and molecular design prediction of materials.²⁷ In these tasks, large language models determine the next course of action by reasoning over the information available in their environment.^{24,26,27}

With this in mind, a multi-agent approach for the search, discovery, and simulation of potential alloys suitable for additive manufacturing. These tools are built to adhere to the standards established in the Model Context Protocol (MCP)²⁸ and can be easily integrated into any client with an MCP interface.

2 Methodology

2.1 Calculation of Thermophysical Properties

For this task, given an arbitrary element composition of a specific alloy, Thermo-Calc¹⁷ is expected to provide the relevant material properties of density, thermal conductivity, specific heat capacity, electric resistivity, and the liquidus and solidus phase transition temperatures. Thermo-Calc utilizes a CALPHAD based solver to calculate equilibrium phase diagrams and extrapolate properties along with the material property databases to assist with obtaining thermophysical properties for various alloys. The platform also includes their TC-Python SDK allowing for programmatic use of the features, providing an interface for the creation and binding of agentic tools callable via MCP.

With the Thermo-Calc’s property diagram calculation function, a composition of elements is provided to generate a property diagram to extract material properties. Compositions consist of the mass fraction of individual elements and for commonplace alloys, a map of their elemental compositions is obtained from existing literature sources.^{29–43} In this process, a suitable database (one of TCFE14, TCNI12, TCAL9, TCTI6, and TCHEA7, or PURE5⁴⁴) is selected to obtain the necessary phase and transport properties with the appropriate SI units. Database selection is determined through matching an alloy’s primary element compo-

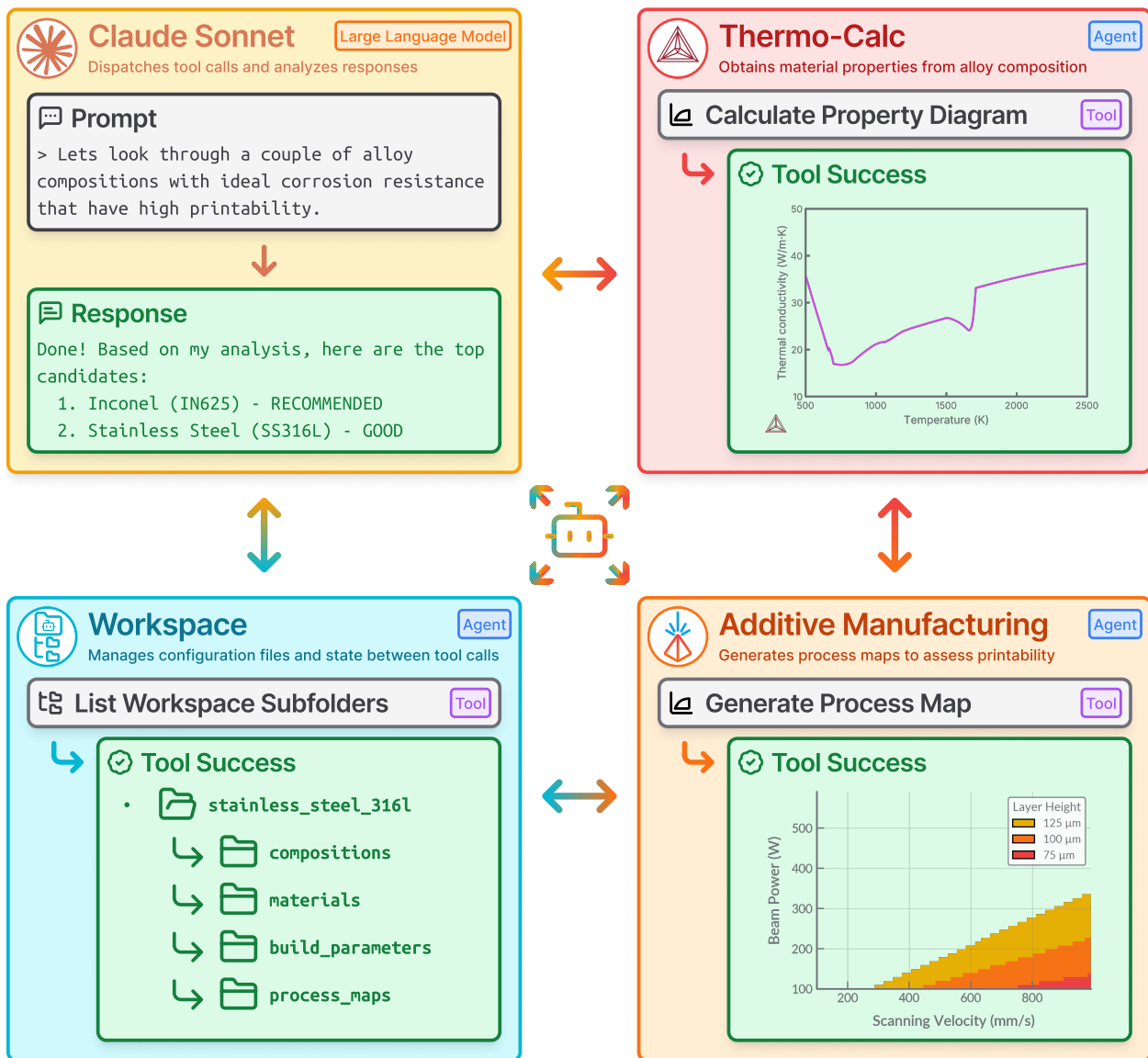


Figure 1: **(Top Left)** An input query for alloy compositions regarding the printability of an additively manufactured part suitable for its intended use case is provided to Claude Sonnet. This Large Language Model (LLM) calls the tools necessary to generate and analyze each potential alloy compositions, providing a response of candidates ranked by their content of their lack of fusion fusion regimes. **(Top Right)** Thermo-Calc allows for the retrieval of material properties for an arbitrary alloy composition, for instance thermal conductivity, to be used in down stream printability calculations. **(Bottom Left)** Workspaces provide a way for each of the tools to effectively communicate with one another and handles state management and file organization. **(Bottom Right)** Tools managed by the Additive Manufacturing subagents then utilize the calculated material properties from the Thermo-Calc subagent to generate a lack of fusion process map to send back to the LLM for analysis and final recommendation.

sition to its database counterpart (i.e. composition of Ni \geq 0.30 uses the TCNI12 database). The provided compositions and database values are then utilized in equilibrium calculations where the minimization of Gibbs Free Energy is iteratively calculated until convergence is met.^{45,46}

Solidus and liquidus phase transition temperatures are extrapolated through tracking the liquid volume fraction. A one-dimensional temperature sweep is performed to find a point where the liquid fraction moves from approximately 0 to 1. The default arguments for the minimum and maximum temperature ranges are 500 K and 3500 K respectively. The obtained solidus and liquidus temperatures are utilized in subsequent tasks to obtain material properties from the proposed alloy. Density ($\rho = B/V$) and specific heat capacity are obtained through Thermo-Calc's user function using the ratio of mass (B) to volume (V) and the temperature derivative of molar enthalpy denoted as `HM.T` respectively. Thermal conductivity and electrical resistivity are built-in thermodynamic quantities and can be readily obtained at a given temperature. The melting temperature is taken as the average between the solid and liquidus phases.

Absorptivity is approximated using the series expansion for emissivity in a direction normal to the surface (Equation 1).⁴⁷ Here, $\varepsilon_\lambda(T)$ denotes the emissivity at a given wavelength (λ) and temperature (T) where the conductivity of a metal (γ) is expected in units of $(\Omega \cdot \text{cm})^{-1}$.

$$\varepsilon_\lambda(T) = \frac{0.365}{\sqrt{\gamma\lambda}} - \frac{0.0667}{\gamma\lambda} + \frac{0.006}{\sqrt{(\gamma\lambda)^3}} - \dots \quad (1)$$

Since resistivity (ρ) and conductivity (γ) are reciprocal properties ($\gamma = \frac{1}{\rho}$), Equation 1 can be modified to accept our computed electrical resistivity value and near infrared wavelength of 1070 nm. (Equation 2).

$$\varepsilon_\lambda(T) = 0.365\sqrt{\frac{\rho}{\lambda}} - 0.0667\frac{\rho}{\lambda} + 0.006\sqrt{\left(\frac{\rho}{\lambda}\right)^3} - \dots \quad (2)$$

The calculated material properties of absorptivity, thermal conductivity, liquidus and solidus phase transition temperatures, density, and specific heat capacity are saved as a common material configuration compatible with the `additive-manufacturing` package. These values will then be utilized with the tools there for initialization and generation of a lack of fusion process map to evaluate the printing feasibility of these material properties.

2.2 Lack of Fusion Defect Prediction

Defects created within the laser powder bed fusion process can arise through various means and affect the final part's material and mechanical properties.⁴⁸⁻⁵⁰ This includes defects such as porosity, microstructural inhomogeneity, and inclusions which can result in degraded performance in fatigue life as well as mechanical strength.^{48,51} The source of these defects can be attributed to at least one of the following process map defect regimes of either Lack of Fusion (LoF), Keyholing, or Balling.^{48,52} Of these defects, porosity from lack of fusion presents a significant risk to the fatigue life as it provides a starting point for cracks to nucleate from.^{51,53}

The criterion for lack of fusion is primarily concerned with overlap between subsequent melt pool tracks, where adjustments to the hatch spacing along with layer height contribute determine the amount of unfused powder within the build.^{48,54} This is modeled by with Equation 3^{48,54,55} where computed ratios greater than 1 are expected to exhibit lack of fusion defects.

$$\left(\frac{Hatch\ Spacing}{Melt\ Pool\ Width} \right)^2 + \left(\frac{Layer\ Height}{Melt\ Pool\ Depth} \right)^2 \leq 1 \quad (3)$$

Hatch spacing and layer height are independent process parameters that are prescribed for the build process. Melt pool dimensions of depth and width are physical values that obtained from either cross-sectional measurements of the scan track⁵⁶ or modeling using solvers such as that of the Rosenthal^{19,54,57} equation (Equation 4). In this equation a number

of assumptions are made which include a melt pool in conduction mode, a point heat source, and temperature-independent thermal properties.^{19,54}

$$T = T_{\infty} + \frac{Q}{2\pi kR} \exp\left(\frac{V(z - R)}{2\alpha}\right) \quad (4)$$

In Equation 4, the local temperature T (K) is obtained at a distance z (m) along the travel direction for a radial distance R (m) from the beam position.^{19,57} Additional factors such as the temperature of the plate T_{∞} (K), applied power Q (W), scan speed V (m/s), thermal diffusivity α (m²/s), and thermal conductivity k (W/mK) utilized to provide an approximate calculation of the temperature field.^{19,57} Thermal diffusivity ($\alpha = \frac{k}{\rho C_p}$) can be obtained from thermal conductivity k (W/mK), density ρ (kg/m³), and specific heat capacity C_p (J/kg·K). Radial distance R is the combined coordinate of $R^2 = z^2 + r^2$ where z (also $-\xi$) is the distance along the center line.

$$z = R + \frac{2\alpha}{V} \ln\left(\frac{2\pi kR\Delta T}{\epsilon P}\right) \quad (5)$$

Given the liquidus temperature of a material, Equation 4 can be rearranged to provide the bounds of the melt pool. This is shown with Equation 5, where $\Delta T = T_{melting} - T_{initial}$ and ϵ represents the dimensionless absorptivity value. The length of the melt pool can be obtained by calculating the length of the temperature field in front and tailing the heat source. The tailing length (Equation 13) of the heat source can be obtained from setting the z to R and then solving for R as seen with its derivation included in Appendix B. This provides a stop point when passing R values into Equation 5 with a step size of 1 μm when calculating the bounds, recording the maximum to use as the melt pool dimensions.

2.3 Model Context Protocol

The Model Context Protocol (MCP) is a standard introduced by Anthropic⁵⁸ which provides guidelines for used functionality such as tool calling and resource querying; Particularly

suitable for agentic tasks.^{28,59-61} Along with these features, MCP is compatible with the wider ecosystem of LLM providers with integrations in Software Development Kits (SDKs) developed by Anthropic,⁵⁹ OpenAI,⁶² Google,⁶³ and others.⁶¹

2.3.1 Tools

Tools are the primary means in which an LLM is able to perform actions via MCP, invoking external Application Programming Interfaces (APIs) or function calls with the user's approval.⁵⁹⁻⁶¹ Complexity of these tool calls can range from simple stateless actions (network requests to external APIs) or long-lived function operations (simulation runs).⁵⁹ Using the MCP Python SDK,⁵⁹ these tools can be exposed to the LLM with the appropriate decorator function configuration as seen in Appendix A. A minimal configuration consisting of the decorator wrapping a tool function is sufficient to register a tool for an LLM. However, additional annotations such as type declarations, docstring descriptions, and structured outputs significantly improve the model's comprehension and proper utilization of the defined tool.

2.3.2 Resources

Resources provide the LLM capability to search for relevant information regarding a given task. Similar to GET requests established within the Hypertext Transfer Protocol (HTTP),⁵⁹ this allows for the query of information stored within databases, filesystems, or other means to be accessible to the LLM.^{60,61} This is particularly useful during the tool calling process as it provides environmental state information regarding around the model. However, during experiments the LLM's utilization of the resource functionality proved unreliable and tools implementing the same functionality of each resource displayed consistently reliable responses.

```

* Welcome to Claude Code!

> Lets look through a couple of alloy
compositions with ideal corrosion
resistance that have high printability.

• Update Todos
✓ Get list of available alloy
✓ Create workspace for alloy analysis
✓ Analyze compositions of corrosion-
resistant alloys
✓ Generate process maps to evaluate
printability
✓ Compare candidates and recommend
best option

Done! Based on my analysis, here are the
top candidates:
1. Inconel (IN625) - RECOMMENDED
2. Stainless Steel (SS316L) - GOOD

```



Figure 2: **(Left)** Claude Code provides an interface for integrating agentic tools with Claude Sonnet LLM, allowing for natural language input to execute tasks and response analysis. **(Right)** Streamlined summary of tool executions and analysis from the prompt given to Claude Code utilizing subagents for Additive Manufacturing, Thermo-Calc, and Workspace.

2.4 Agentic Tools

Tools developed for this application are separated into three different MCP Servers with Python Package Index (PyPi)⁶⁴ identifiers: `additive-manufacturing`, `thermo-calc`, and `workspace-agent`. Each of these packages maintain their own MCP server tools and *Sub-agent*⁶⁵ (a simple markdown file providing additional context and system prompts to guide tool usage) and are capable of standalone usage. Claude Code⁶⁶ provides a platform for coupling these tools into a multi-agent environment utilizing Claude Sonnet 4⁶⁷ as the primary large language model for orchestrating tool calls and performing response analysis.

2.4.1 workspace-agent

The `workspace-agent` package, abbreviated to `wa` internally, is responsible for the initialization and management of workspaces within the context of tool calls. It primarily acts as a state management tool for storing JSON serialized class objects and deserializing the

stored JSON files to use within tools. This approach allows for different tools to use the same Python class methods and state since the input types to each tool are limited to primitives accessible via command line. Thus, filename references to serialized JSON files are provided as inputs to be loaded and deserialized within each tool since string, int, and formatted list and dict types are valid inputs to tools but Python instances of classes or functions are not.

Workspaces can be initialized via tool call (Figure 3) and are subdivided into top-level subfolders (i.e. `compositions`, `materials`, `process_maps`, etc.) containing state and responses for a given domain. Tools to list existing subfolders and their contents act as guides to help the LLM navigate through potential tool input arguments narrow the search window to the most applicable candidates. In addition to being listed as tools, functionality to list subfolders and their content are also exposed as resources accessible via MCP allowing for the LLM and user interface to obtain this information implicitly via syntax (i.e. `@workspace://{workspace}/{subfolder}/`).

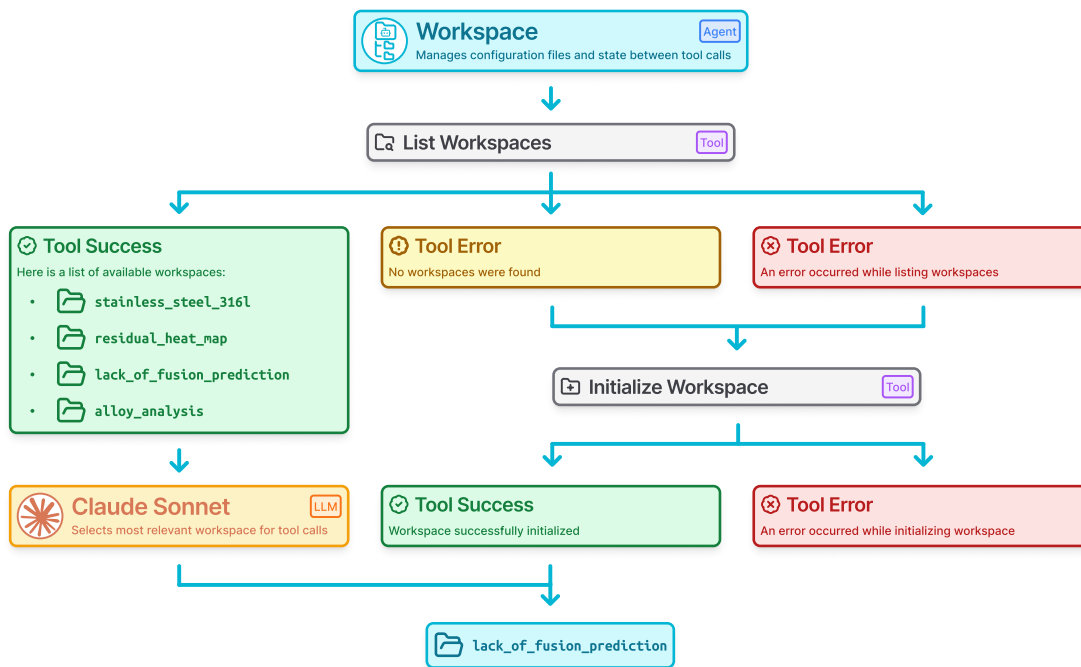


Figure 3: A simple tool calling procedure within the Workspace subagent for the task of finding or initializing a workspace. Here an initial tool call is made to list available workspaces and if none are found, a new workspace is created. This newly initialized workspace or the most relevant selected by Claude Sonnet is included in the successful response object.

The MCP server for workspaces operates independently, acting without direct knowledge of other installed MCP servers relying only on the LLM context to provide the appropriate arguments for workspace names and subfolders to navigate. This architecture allows for the other MCP servers to utilize workspace functionality preventing the issue of tool overlap between packages. This opinionated approach allows for MCP servers that utilize `workspace-agent` to share workspace subfolders such that the output of one MCP server's tool can be utilized as an input to another MCP server tool.

2.4.2 `thermo-calc`

For this project, the authors developed and published a package with the PyPi⁶⁴ identifier `thermo-calc` (aliased internally as `tc`) to facilitate the installation and use of Thermo-Calc's TC Python module.¹⁷ Along with these installation scripts, Command Line Interface (CLI) and MCP bindings were also implemented for a subset of TC Python's functionality, those of which are outlined in Section 2.1. With the set of tools managed by the `thermo-calc` subagent, the material properties of a given alloy composition can be calculated and saved to a shared material configuration that the tools from `additive-manufacturing` can then utilize for process map generation.

In this process, an arbitrary alloy composition element or an existing element name is provided to the large language model in order to create an alloy composition file (Figure 4). An alloy composition file is produced by serializing provided element proportions to a JSON file consisting of element keys and mass fractions. (i.e. `{"Fe": 0.9, "C": 0.1}`) Both approaches eventually utilize the alloy composition schema tool, however if the subagent is provided a generic alloy name, it utilizes tools to list known alloys and obtain their compositions to then pass into the alloy composition schema tool.

Once the alloy composition is obtained, the TC-Python API is called to instantiate a server to calculate the Property Diagram for the given set of elemental compositions and temperature range. This returns a `PropertyDiagramResult` which is then saved for later

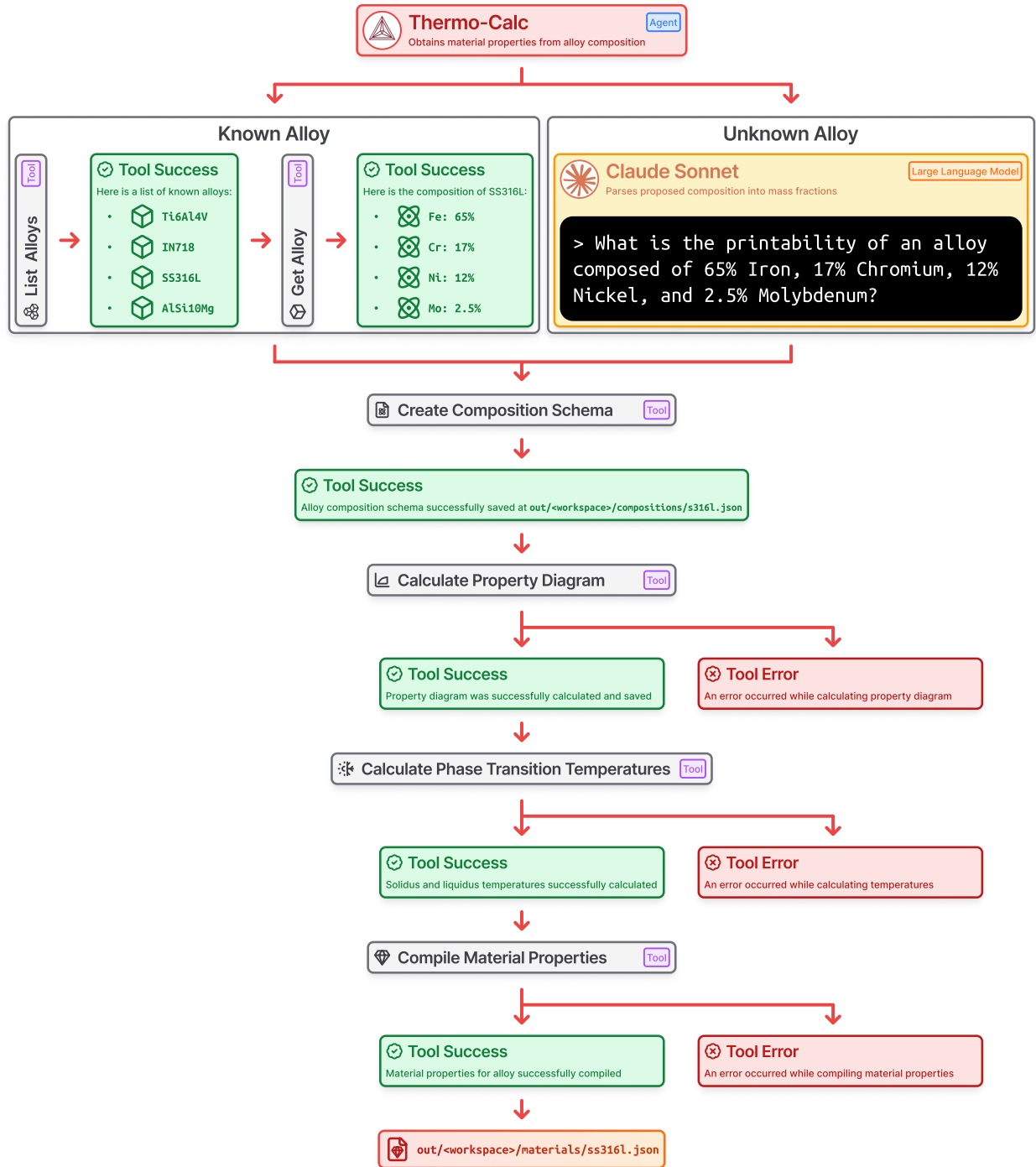


Figure 4: Flow diagram outlines the expected tool calling procedure for the Thermo-Calc subagent. In this example the material properties for Stainless Steel are extracted from the calculated property diagram of the alloy’s elemental composition. Composition is obtained from a look-up table of known alloys or provided directly to the agentic system and parsed into mass fractions using Claude Sonnet. This process generates a schema file with alloy’s material properties recorded for downstream use with other tools.

use when calculating phase transition temperatures and other material properties. In a separate tool call, the `PropertyDiagramResult` is loaded for the volume fraction calculation of the liquid phase which the liquidus and solidus phase transition temperatures can be extracted from. The liquidus, solidus, and melting (midpoint between liquidus and solidus) are then saved into a phase transitions temperatures configuration file and utilized later in the calculation of other material properties and serialization of the material schema.

The previously calculated values are managed by `workspace-agent` package and are saved in the `property_diagrams`, `phase_transition_temperatures`, and `compositions` subfolders respectively. The relevant configurations are loaded from these subfolders into the material compilation tool which determines the values for the remaining material properties, those being specific heat capacity, density, thermal conductivity, and absorptivity. These values are instantiated as `Material` class and serialized into the `materials` subfolder as a JSON file for lack of fusion process map generation.

2.4.3 additive-manufacturing

The `additive-manufacturing` (`am`) package provides a set of tools to assist with the additive manufacturing build process, currently built around providing feed forward solutions to predict potential build defects and gauge its feasibility. Of the available features, the experimental setup primarily utilizes the package's process map generation capabilities in order to predict potential lack of fusion defect regimes. The exact process for computing the melt pool dimensions necessary for determining the lack of fusion defect regime is outlined in Section 2.2, but in short, melt pool dimensions are calculated using an equation from Rosenthal¹⁹ and fed into the lack of fusion defect criterion (Equation 3) to classify the input process parameter combination. In the current implementation classifications are limited to within or outside the lack of fusion defect regime as the analytic solution only works for conduction mode and cannot model melt pools in keyhole mode.¹⁹

Process map generation is managed by the additive manufacturing subagent responsible

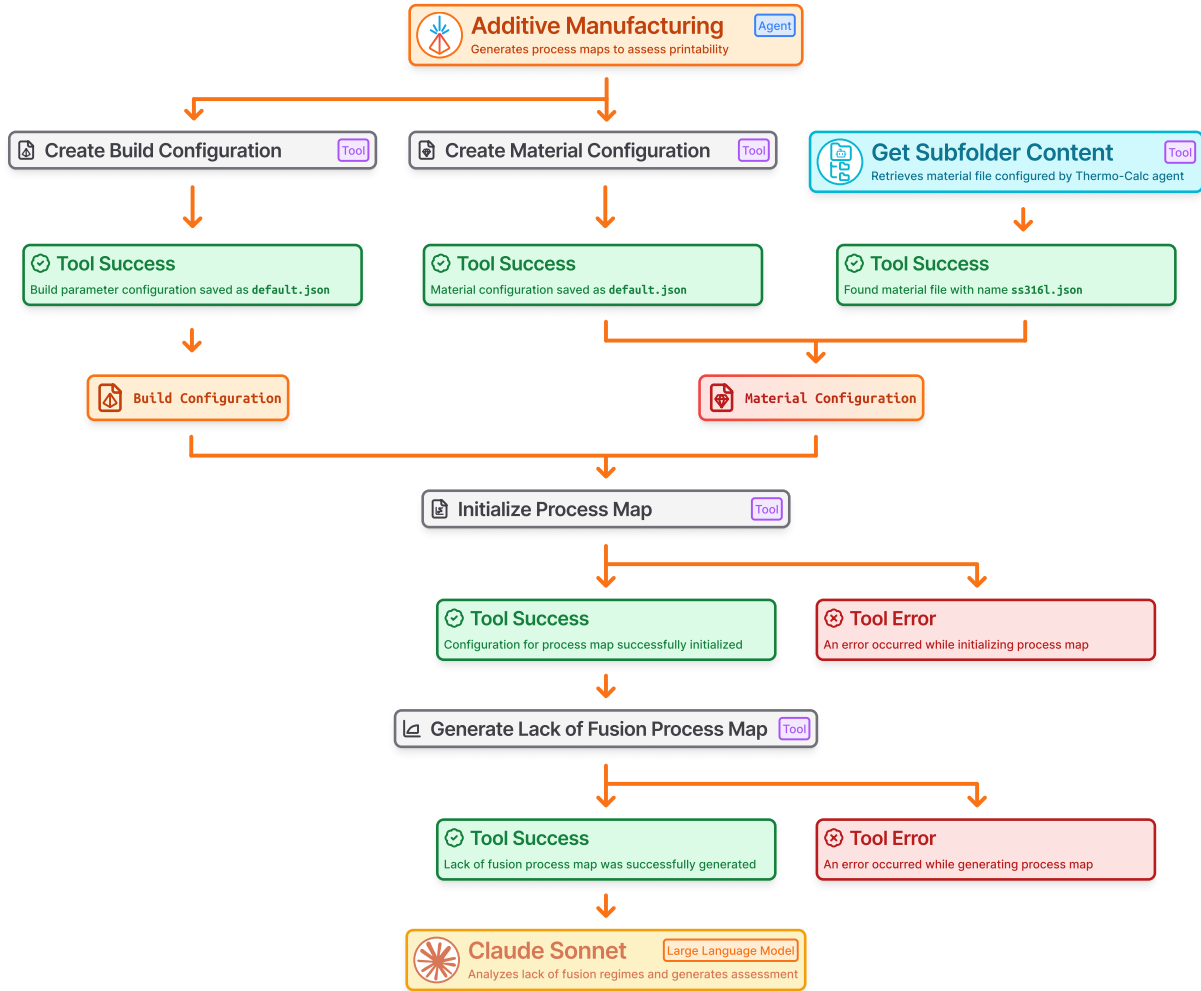


Figure 5: Diagram outlines expected tool calling procedure for additive manufacturing sub-agent for the task for generating and analyzing a lack of fusion process map. Build and material configurations are required to initialize a process map, the latter of which can be obtained from the Thermo-Calc subagent or manually configured by the additive manufacturing subagent. Initializing the process map provides override ranges for power and velocity build parameters for melt pool depth calculations. The tool generates the process map and a response consisting of power and velocity configurations that potentially exhibit lack of fusion defects. Claude Sonnet analyzes this response and provides suggestion for optimal build parameters.

for the relevant tools within its MCP server (Figure 5). To achieve this configuration files for desired materials and build parameters need to be created before the process map can be initialized and generated. Material configuration contains material dependent properties such as density, thermal diffusivity, thermal conductivity, and liquidus and solidus phase transition temperatures to name a few. Build configuration manages values such as beam power, scan velocity, layer height, and hatch spacing. These configuration files are utilized by the process map initialization tool which creates the subfolder for storing process map results and the process map configuration file for overriding build parameter configurations of beam power and scan velocity. Instead of a single scalar value, process map configuration file overrides the build configuration file with a range of values as to use the same material and build configurations when calculating defect regimes but with either a different power or velocity. The default process map range for power and velocity is 100 to 1000 with steps every 100 W or mm/s respectively. With this, the necessary calculations are performed to obtain lack of fusion regimes for 2 layer heights ($-25 \mu m$ and $+25 \mu m$) in addition to the prescribed layer height within the provided range of process parameters.

The Command Line Interface (CLI) provides the basic means of interaction with the `additive-manufacturing` package, however with its MCP integration, inputs and arguments can be left unstructured and functionality is accessible through just natural language when utilized as tools within an MCP server. In addition to natural language functionality, its integration with an LLM (i.e. Claude Sonnet) augments the capabilities of the user enabling easy evaluation of follow-up changes and LLM enabled analysis and feedback of computed results. Through the `workspace-agent` package, material configurations generated with the `thermo-calc` package can be utilized for the generation of process maps, allowing for the end-to-end functionality of proposing alloy compositions to analyzing their lack of fusion process map.

2.5 Experiments

Several experiments were performed to investigate the capability of the agentic system. Each experiment consists of a simple prompt regarding the desired alloy or material properties to explore (as shown in Figure 2) with the expected generation of a lack of fusion process map along with analysis and suggestion of potential printing parameters to implement. The whole of these experiments aims to cover the wide range of potential use case scenarios supported with the provided tools ranging from known and unknown alloys to searching and assessing alloys with a desired material property characteristic.

2.5.1 Known Alloys

Within the scope of known alloys, the system is expected to adhere to the established approach to obtaining a process map for a given material compositions with the caveat of obtaining these alloy composition from a provided dictionary. In this task it is expected that the LLM only acts to dispatch tools and interpret their subsequent response. This approach would be evaluated on a subset of the known alloys which include: Stainless Steel 316L, Titanium, Inconel, Aluminum, Tool Steel, Iron, Copper, Hastelloy X, K500, Tungsten, Bronze, and Aluminum 7050.

2.5.2 Material Property Search

For an open ended task, such as that encountered during the search for an alloy composition with specific desirable material properties, the large language model is utilized more. In this case, a similar approach to that of the known alloys is taken to determine an alloy's printability with an initial query given to the LLM to provide a list of candidates with the desired material properties. This included properties such as corrosion resistance, fatigue life, yield stress, Young's modulus, fracture toughness, hardness, and ductility.

2.5.3 Unknown Alloys

Compositions outside that of the known alloys were also included in this investigation. With this, an arbitrary combination of elements along with their prescribed proportions are provided to the system. The LLM is able to interpret this combination of elements into their respective mass fractions and call the relevant tools to determine its printability. The system was evaluated with compositions ranging from slight modifications of known alloys to completely arbitrary combination of elements to element compositions proposed by the LLM.

3 Results

For the known alloys, the lack of fusion process map was obtained using the provided alloy composition. In these experiments, the large language model is responsible for the selection of build parameters along with defining the appropriate process map range within the power and velocity process parameters. Of the 12 alloys this experiment was performed upon, 11 were able to produce a suitable lack of fusion process map (Figure 6). The one failure in this case occurred with the Tool Steel prompt which resulted in the process hanging while utilizing the property diagram calculation tool.

Validation of the lack of fusion predictions of known alloys indicate satisfactory overlap between those generated by additive manufacturing subagent and that found within published literature. In a study by Ghanadi et al.,⁶⁸ lack of fusion was observed at laser powers between 50 to 150 Watts and scan speeds of 700 mm/s to 1200 mm/s when conducted with a prescribed layer height of $25\mu\text{m}$ and hatch space of $40\mu\text{m}$. These process parameters are similar to those implemented using the additive manufacturing subagent ($50\mu\text{m}$ hatch spacing and $30\mu\text{m}$). Although the generated process map for Inconel 718 (Figure 6) denotes a slight under prediction of lack of fusion compare to that of the literature, this can be attributed the more general applicability of Rosenthal's equation.¹⁹ The generated process map for Stainless Steel 316L (SS316L) matches the lack of fusion regimes outlined in the literature,

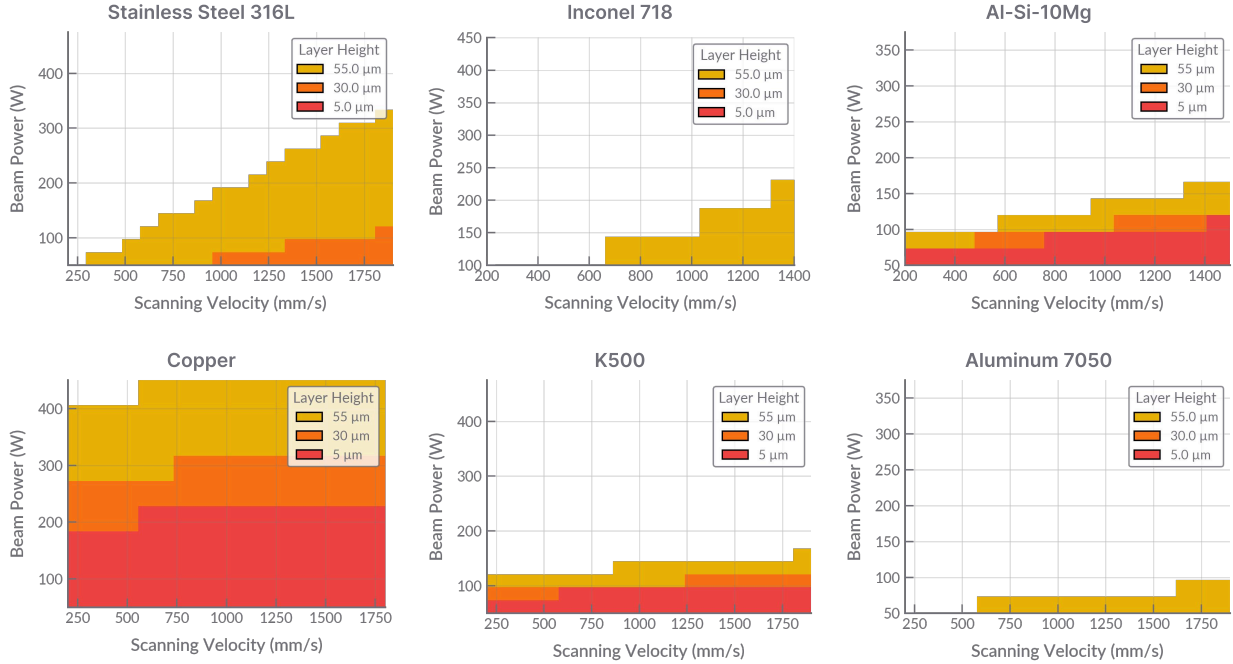


Figure 6: Lack of fusion process maps for a selection of known alloys with default hatch spacings of $50\mu\text{m}$.

with unfavorable process windows at lower powers and higher velocity combinations.^{69–71} Ahmed et al.⁶⁹ encounters high densification of SS316L at power and velocity combinations of (150 W, 500 mm/s), (200 W, 700 mm/s), (250 W, 900 mm/s), and (300 W, 1100 mm/s), matching that presented in Figure 6. Similar agreement is seen with copper based alloys where the high power (upwards of 400 W) is necessary to achieve adequate melting.^{72,73}

When prompted to search for an alloy with a specific material property, the LLM reasons through number of potential candidates and selects a couple to evaluate. The same procedure is taken for generating process maps for each alloy candidate the results of which are evaluated and compared with emphasis towards printability (Figure 7). Of the 9 investigated material properties, the agentic system failed to produce process maps for only one of the cases. The failure case occurred while comparing creep resistance of various alloys, specifically when attempting to generate the process map investigating the nickel based superalloy, Mar-M 247. Besides this exception, all prompts were successful in creating lack of fusion process maps and performing analysis and recommendations based on the printability

of each candidate.

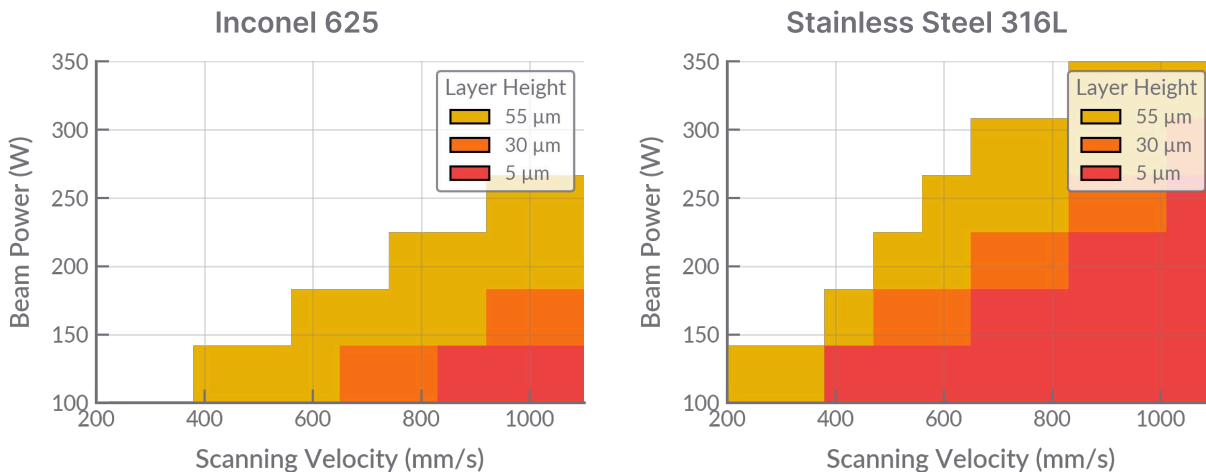


Figure 7: Comparison of lack of fusion process maps of between Inconel 625 and Stainless Steel 316L for corrosion resistant applications. Between these two candidates, the LLM ultimately recommended the use of Inconel 625 for its smaller lack of fusion regime.

For the application of corrosion resistance, the additive manufacturing subagent recommendation of Inconel 625 aligns with the findings from multiple literature sources.^{74–76} In a study by Zhang et al.,⁷⁴ the authors investigate corrosion resistance of Inconel 625 and Stainless Steel 316L hybrid alloys under the application of hydrofluoric acid. Inconel is stated to have greater corrosion resistant properties than that of Stainless Steel 316L however, due to its higher Nickel and Chromium content the manufacturing cost is higher as well.⁷⁴ Process parameter combinations used with Inconel 625 range from 175 W and 500 mm/s⁷⁷ to 1000 W and 600 mm/s,⁷⁴ all of which are valid process parameters within the prediction of the additive manufacturing subagent.

In the case of unknown alloys, compositions are directly evaluated and in some instances produce rather extreme process maps. Of the 10 conducted experiments, 8 were successfully able to produce process maps with 2 failing due to the nature of the alloy composition. Although the system accepts any composition of elements, most arbitrary combination of elements are unsuitable for printing and practical use. As such, slightly adjusting known alloy combinations produces more suitable lack of fusion regimes as seen in the cases where

Molybdenum is removed for Stainless Steel 316L or Inconel 625 (Figure 8).

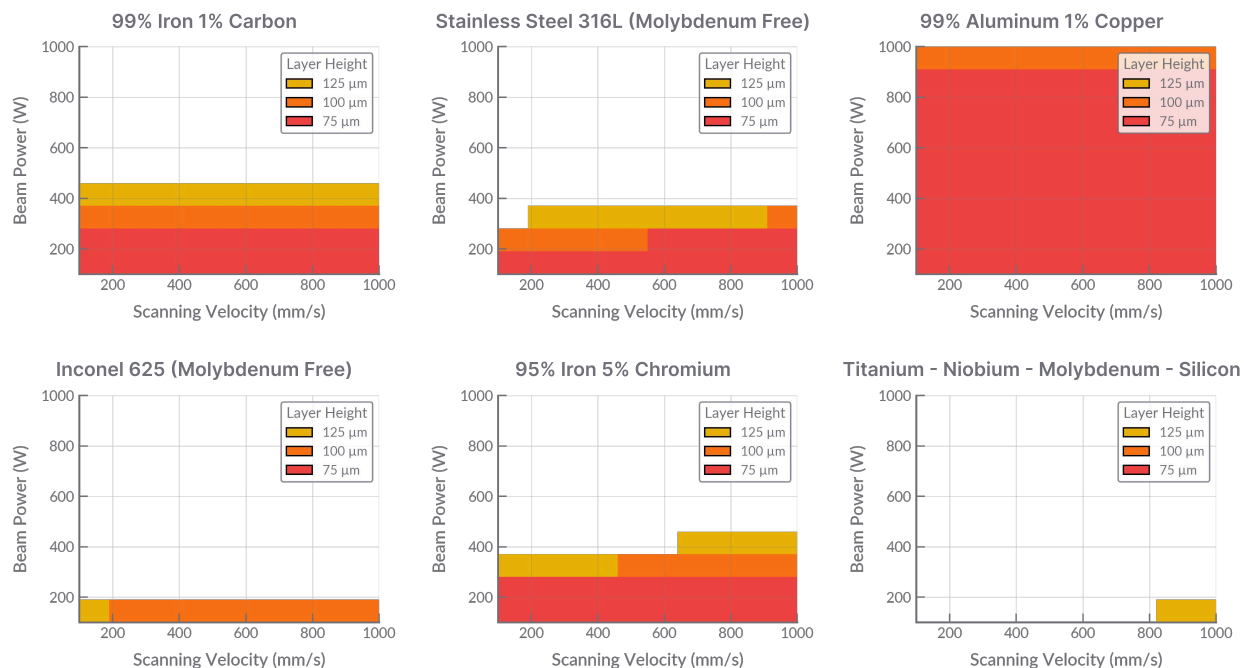


Figure 8: Lack of fusion process maps for arbitrary element compositions, slightly modified known alloy compositions, and LLM proposed composition.

4 Discussion

In this agentic system, all tasks are completed with tools performing deterministic actions; the large language model merely orchestrates and analyses the response of dispatched tool calls. As a result, fidelity of the system’s predictions relies primarily on the accuracy of the developed tools. To that point, this work limits its process map prediction to the lack of fusion regime as it utilizes a conduction mode limited analytical approach to obtain melt pool dimensions.¹⁹ With these separation of concerns, determining the source of invalid predictions is simplified where incorrect evaluation of results can be attributed to the large language model and production of inaccurate predictions can be assigned to the tool.

Within the experimental trials a few prompts produced incorrect results as such was the case in evaluating a material with optimal hardness. In this case the lack of fusion

process maps were correctly generated however the LLM recommended the use of Enhanced Maraging Steel over the other two candidates (Figure 9). From visually interpreting the process maps, it is clear that Enhanced Maraging Steel has the largest lack of fusion regime when compared to its counterparts. One potential cause of this misinterpretation could be attributed to the response data structure returned to the LLM after a tool call. Since the lack of fusion regimes are returned as power and velocity combinations within a list of tuples (i.e. $[(100, 100), (150, 100), \dots]$), the LLM may have misinterpreted these values to be valid process windows rather than lack of fusion regimes. Proper key names and serializing of results would help reduce these types of LLM mistakes.

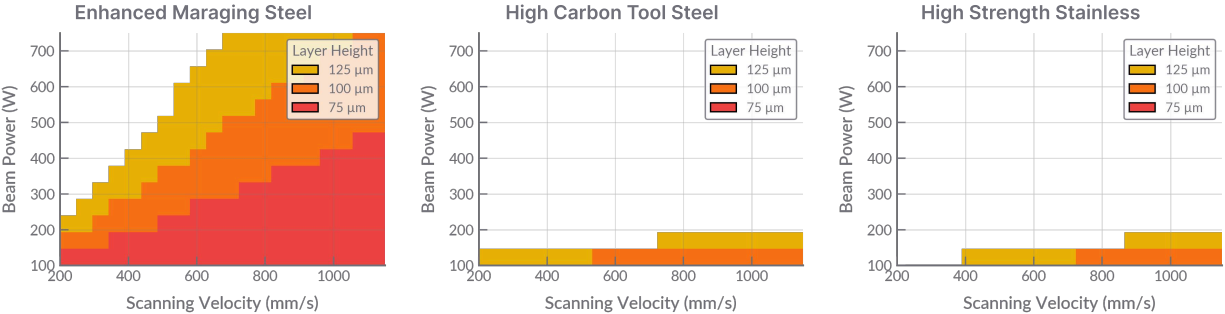


Figure 9: High hardness alloy candidates with their respective lack of fusion process maps. LLM makes an error by recommending Enhanced Maraging Steel over High Strength Stainless Steel for its printability.

The deterministic nature of these tools does present the question of the benefit of introducing an LLM into the system, as if the tools can work on their own individually, what would be the purpose of including an LLM into the architecture. This is a valid concern as the common workflows of each tool can be connected to each other through a parent script, achieving the same effect. However, the inclusion of an LLM and the separation of tools into their own subagents allows for several unique capabilities. The most apparent of these is the utilization of natural language when interacting with the developed tools. This allows the user to directly interact with the available tooling without explicitly adhering to the strict syntax and argument guidelines required by the CLI. Another is the LLM’s ability to analyze results providing user interpretive feedback on a tool’s response. This supports

another key ability of LLM agents which is to establish a feedback loop and respond to changes within its context. The integration of LLM Agents within the developed tools not only enhances the user experience with these tools but establishes an automation framework enabling researcher to efficiently utilize their available tools.

5 Conclusion

The integration of tool calls through frameworks such as MCP allows for effective utilization of LLM Agents for the task of alloy discovery within additive manufacturing. This augments a researcher's ability to investigate new alloys through enabling the use of natural language while working with tools from the `thermo-calc` and `additive-manufacturing` packages. In addition, these tools can leverage the generalized knowledge of LLMs through querying its large base of knowledge and reason through tasks such as finding suitable alloy compositions with desirable material properties. This work sets the foundation for complex tool usage and automated research within the additive manufacturing field.

6 Future Work

Although the authors have provided a comprehensive study on the use of agentic tools within the additive manufacturing space, there remain a couple of aspects to this work that would benefit from further research. One of which is the inclusion of the other keyhole and balling regimes within the process map, however, this requires a modeling solution that extends beyond melt pools in conduction mode. Other additions would further implement features from Thermo-Calc's TC-Python module into MCP tools to allow for agents to utilize more indepth functionality. Lastly, validation of this MCP based approach on additional models outside those developed by Anthropic would help provide a baseline to the performance expected from this agentic system.

Appendix A Model Context Protocol Example Tool

```
1 @app.tool(  
2     title="Run Layer with Solver",  
3     description="Runs solver on a segments file (segments file  
4         should be one layer) and saves the generated meshes.",  
5     structured_output=True,  
6 )  
7 def solver_run_layer(  
8     workspace: str,  
9     segments_foldername: str,  
10    layer_number: int,  
11    build_config_filename: str = "default.json",  
12    material_config_filename: str = "default.json",  
13    mesh_config_filename: str = "default.json",  
14    run_name: str | None = None,  
15 ) -> Union[ToolSuccess[Path], ToolError]:  
16     """  
17     Runs solver for segments at a specified layer number.  
18     Args:  
19         workspace: Folder name of existing workspace  
20         segments_foldername: Folder name of where segments are  
21             expected to be found.  
22         layer_number: Layer number to run solver on, typically  
23             starts from 1. For testing out, try skipping the first  
24             several layers as those sometimes don't include part  
25             geometry.  
26         distance_xy_max: Maximum segment length when parsing (  
27             defaults to 1.0 mm).  
28         build_config_filename: build config file to use with solver.  
29         material_config_filename: material config file to use with  
30             solver.  
31         mesh_config_filename: mesh config file to use with solver.  
32         run_name: Name of folder to save generated meshes at,  
33             typically autogenerated.  
34     """  
35     ...
```

Figure 10: Example tool implementation shown via Solver tool defined in additive-manufacturing package.

Appendix B Melt Pool Length

Rosenthal's equation¹⁹ can be rewritten to provide the bounds for the melt pool. If z is substituted with R , the width of the melt pool shrinks to zero and becomes the furthest point in the melt pool.

$$z = R + \frac{2\alpha}{V} \ln \left(\frac{2\pi k R \Delta T}{\epsilon P} \right) \quad (6)$$

$$R = R + \frac{2\alpha}{V} \ln \left(\frac{2\pi k R \Delta T}{\epsilon P} \right) \quad (7)$$

$$0 = \frac{2\alpha}{V} \ln \left(\frac{2\pi k R \Delta T}{\epsilon P} \right) \quad (8)$$

Since the coefficient term $\frac{2\alpha}{V}$ will be a non-zero value, ignore this term to simplify calculation.

$$\frac{2\alpha}{V} \neq 0; 0 = \ln \left(\frac{2\pi k R \Delta T}{\epsilon P} \right) \quad (9)$$

Taking the exponential of both sides and solving for R produces the following equation that provides the expected length of the melt pool from the heat source.

$$e^{\ln \left(\frac{2\pi k R \Delta T}{\epsilon P} \right)} = e^0 \quad (10)$$

$$\frac{2\pi k R \Delta T}{\epsilon P} = 1 \quad (11)$$

$$2\pi k R \Delta T = \epsilon P \quad (12)$$

$$R = \frac{\epsilon P}{2\pi k \Delta T} \quad (13)$$

References

- (1) Bandyopadhyay, A.; Heer, B. Additive manufacturing of multi-material structures. *Materials Science and Engineering: R: Reports* **2018**, *129*, 1–16.
- (2) Bandyopadhyay, A.; Traxel, K. D.; Lang, M.; Juhasz, M.; Eliaz, N.; Bose, S. Alloy design via additive manufacturing: Advantages, challenges, applications and perspectives. *Materials Today* **2022**, *52*, 207–224.
- (3) Ghafarollahi, A.; Buehler, M. J. AtomAgents: Alloy design and discovery through physics-aware multi-modal multi-agent artificial intelligence. 2024; <http://arxiv.org/abs/2407.10022>, arXiv:2407.10022 [cs].
- (4) Tammam-Williams, S.; Todd, I. Design for additive manufacturing with site-specific properties in metals and alloys. *Scripta Materialia* **2017**, *135*, 105–110.
- (5) Polonsky, A. T.; Pollock, T. M. Closing the science gap in 3D metal printing. *Science* **2020**, *368*, 583–584, Publisher: American Association for the Advancement of Science.
- (6) Sames, W. J.; List, F. A.; Pannala, S.; Dehoff, R. R.; Babu, S. S. The metallurgy and processing science of metal additive manufacturing. *International Materials Reviews* **2016**, *61*, 315–360, Publisher: SAGE Publications.
- (7) Jadhav, Y.; Berthel, J.; Hu, C.; Panat, R.; Beuth, J.; Barati Farimani, A. StressD: 2D Stress estimation using denoising diffusion model. *Computer Methods in Applied Mechanics and Engineering* **2023**, *416*, 116343.
- (8) Rashid, A.; Gopaluni, A. A Review of Residual Stress and Deformation Modeling for Metal Additive Manufacturing Processes. *Chinese Journal of Mechanical Engineering: Additive Manufacturing Frontiers* **2023**, *2*, 100102.
- (9) Paul, R.; Anand, S.; Gerner, F. Effect of Thermal Deformation on Part Errors in Metal

- Powder Based Additive Manufacturing Processes. *Journal of Manufacturing Science and Engineering* **2014**, 136.
- (10) Xu, Z.; Zhang, H.; Du, X.; He, Y.; Luo, H.; Song, G.; Mao, L.; Zhou, T.; Wang, L. Corrosion resistance enhancement of CoCrFeMnNi high-entropy alloy fabricated by additive manufacturing. *Corrosion Science* **2020**, 177, 108954.
- (11) Pesode, P.; Barve, S. Additive manufacturing of metallic biomaterials and its biocompatibility. *Materials Today: Proceedings* **2022**,
- (12) Pesode, P.; Barve, S. Additive manufacturing of magnesium alloys and its biocompatibility. *Bioprinting* **2023**, 36, e00318.
- (13) Jiao, C.; Xie, D.; He, Z.; Liang, H.; Shen, L.; Yang, Y.; Tian, Z.; Wu, G.; Wang, C. Additive manufacturing of Bio-inspired ceramic bone Scaffolds: Structural Design, mechanical properties and biocompatibility. *Materials & Design* **2022**, 217, 110610.
- (14) Kaufman, L.; Bernstein, H. *Computer Calculation of Phase Diagrams with Special Reference to Refractory Metals*; Academic Press, 1970.
- (15) Gheribi, A. E.; Chartrand, P. Application of the CALPHAD method to predict the thermal conductivity in dielectric and semiconductor crystals. *Calphad* **2012**, 39, 70–79.
- (16) Campbell, C. E.; Kattner, U. R.; Liu, Z.-K. The development of phase-based property data using the CALPHAD method and infrastructure needs. *Integrating Materials and Manufacturing Innovation* **2014**, 3, 158–180.
- (17) Thermo-Calc Software Thermo-Calc Software. 2025; <https://thermocalc.com/>.
- (18) Eagar, T. W.; Tsai, N. S. Temperature fields produced by traveling distributed heat sources. *Weld. Res. Suppl.; (United States)* **1983**, Institution: Massachusetts Institute of Technology, Cambridge Number: CONF-830485-.

- (19) Rosenthal, D. The Theory of Moving Sources of Heat and Its Application to Metal Treatments. *Transactions of the American Society of Mechanical Engineers* **2022**, *68*, 849–865.
- (20) OpenFOAM. 2025; <https://www.openfoam.com/>.
- (21) FLOW-3D. <https://www.flow3d.com/>.
- (22) Zhang, Y.; Zhang, J. Modeling of solidification microstructure evolution in laser powder bed fusion fabricated 316L stainless steel using combined computational fluid dynamics and cellular automata. *Additive Manufacturing* **2019**, *28*, 750–765.
- (23) Strayer, S. T.; Templeton, W. J. F.; Dugast, F. X.; Narra, S. P.; To, A. C. Accelerating High-Fidelity Thermal Process Simulation of Laser Powder Bed Fusion via the Computational Fluid Dynamics Imposed Finite Element Method (CIFEM). *Additive Manufacturing Letters* **2022**, *3*, 100081.
- (24) Jadhav, Y.; Pak, P.; Farimani, A. B. LLM-3D Print: Large Language Models To Monitor and Control 3D Printing. 2024; <http://arxiv.org/abs/2408.14307>, arXiv:2408.14307 [cs] version: 1.
- (25) Ock, J.; Guntuboina, C.; Barati Farimani, A. Catalyst Energy Prediction with CatBERTa: Unveiling Feature Exploration Strategies through Large Language Models. *ACS Catalysis* **2023**, *13*, 16032–16044, Publisher: American Chemical Society.
- (26) Ock, J.; Meda, R. S.; Badrinarayanan, S.; Aluru, N. S.; Chandrasekhar, A.; Farimani, A. B. Large Language Model Agent for Modular Task Execution in Drug Discovery. 2025; <http://arxiv.org/abs/2507.02925>, arXiv:2507.02925 [cs].
- (27) Chaudhari, A.; Ock, J.; Farimani, A. B. Modular Large Language Model Agents for Multi-Task Computational Materials Science. 2025; <https://chemrxiv.org/engage/chemrxiv/article-details/681239c150018ac7c5d5accf>.

- (28) Anthropic Introducing the Model Context Protocol. 2024; <https://www.anthropic.com/news/model-context-protocol>.
- (29) Akbari, P.; Zamani, M.; Mostafaei, A. Machine learning prediction of mechanical properties in metal additive manufacturing. *Additive Manufacturing* **2024**, *91*, 104320.
- (30) Lber, L.; Schimansky, F. P.; Khn, U.; Pyczak, F.; Eckert, J. Selective laser melting of a beta-solidifying TNM-B1 titanium aluminide alloy. *Journal of Materials Processing Technology* **2014**, *214*, 1852–1860.
- (31) Manfredi, D.; Calignano, F.; Krishnan, M.; Canali, R.; Ambrosio, E. P.; Atzeni, E. From Powders to Dense Metal Parts: Characterization of a Commercial AlSiMg Alloy Processed through Direct Metal Laser Sintering. *Materials* **2013**, *6*, 856–869, Publisher: Multidisciplinary Digital Publishing Institute.
- (32) Jelis, E.; Clemente, M.; Kerwien, S.; Ravindra, N. M.; Hespos, M. R. Metallurgical and Mechanical Evaluation of 4340 Steel Produced by Direct Metal Laser Sintering. *JOM* **2015**, *67*, 582–589.
- (33) Sun, G.; Zhou, R.; Lu, J.; Mazumder, J. Evaluation of defect density, microstructure, residual stress, elastic modulus, hardness and strength of laser-deposited AISI 4340 steel. *Acta Materialia* **2015**, *84*, 172–189.
- (34) Yadollahi, A.; Shamsaei, N.; Thompson, S. M.; Seely, D. W. Effects of process time interval and heat treatment on the mechanical and microstructural properties of direct laser deposited 316L stainless steel. *Materials Science and Engineering: A* **2015**, *644*, 171–183.
- (35) Popovich, A.; Sufiarov, V.; Polozov, I.; Borisov, E.; Masaylo, D.; Orlov, A. Microstructure and mechanical properties of additive manufactured copper alloy. *Materials Letters* **2016**, *179*, 38–41.

- (36) Kok, Y.; Tan, X. P.; Wang, P.; Nai, M. L. S.; Loh, N. H.; Liu, E.; Tor, S. B. Anisotropy and heterogeneity of microstructure and mechanical properties in metal additive manufacturing: A critical review. *Materials & Design* **2018**, *139*, 565–586.
- (37) Schmidtke, K.; Palm, F.; Hawkins, A.; Emmelmann, C. Process and Mechanical Properties: Applicability of a Scandium modified Al-alloy for Laser Additive Manufacturing. *Physics Procedia* **2011**, *12*, 369–374.
- (38) Hack, H.; Link, R.; Knudsen, E.; Baker, B.; Olig, S. Mechanical properties of additive manufactured nickel alloy 625. *Additive Manufacturing* **2017**, *14*, 105–115.
- (39) Rodriguez, O. L.; Allison, P. G.; Whittington, W. R.; Francis, D. K.; Rivera, O. G.; Chou, K.; Gong, X.; Butler, T. M.; Burroughs, J. F. Dynamic tensile behavior of electron beam additive manufactured Ti6Al4V. *Materials Science and Engineering: A* **2015**, *641*, 323–327.
- (40) Lu, S. L.; Tang, H. P.; Ning, Y. P.; Liu, N.; StJohn, D. H.; Qian, M. Microstructure and Mechanical Properties of Long Ti-6Al-4V Rods Additively Manufactured by Selective Electron Beam Melting Out of a Deep Powder Bed and the Effect of Subsequent Hot Isostatic Pressing. *Metallurgical and Materials Transactions A* **2015**, *46*, 3824–3834.
- (41) Tan, X.; Kok, Y.; Tan, Y. J.; Descoins, M.; Mangelinck, D.; Tor, S. B.; Leong, K. F.; Chua, C. K. Graded microstructure and mechanical properties of additive manufactured Ti6Al4V via electron beam melting. *Acta Materialia* **2015**, *97*, 1–16.
- (42) Vrancken, B.; Thijs, L.; Kruth, J.-P.; Van Humbeeck, J. Heat treatment of Ti6Al4V produced by Selective Laser Melting: Microstructure and mechanical properties. *Journal of Alloys and Compounds* **2012**, *541*, 177–185.
- (43) Edwards, P.; O’Conner, A.; Ramulu, M. Electron Beam Additive Manufacturing of Titanium Components: Properties and Performance. *Journal of Manufacturing Science and Engineering* **2013**, *135*.

- (44) Saunders, N.; Miodownik, P. The Application of CALPHAD Methods - ScienceDirect. <https://www.sciencedirect.com/science/article/abs/pii/S1470180498800308>.
- (45) Cross Plots for Alloy Design. 2023; <https://thermocalc.com/blog/icme-workflows-using-cross-plots-to-visualize-the-tradeoff-of-properties-in-alloy-c>
- (46) Property Model Calculator. <https://thermocalc.com/products/thermo-calc/property-model-calculator/>.
- (47) Bramson, M. A. *Infrared Radiation*; Springer US: Boston, MA, 1968.
- (48) Gordon, J. V.; Narra, S. P.; Cunningham, R. W.; Liu, H.; Chen, H.; Suter, R. M.; Beuth, J. L.; Rollett, A. D. Defect structure process maps for laser powder bed fusion additive manufacturing. *Additive Manufacturing* **2020**, *36*, 101552.
- (49) Cunningham, R.; Nicolas, A.; Madsen, J.; Fodran, E.; Anagnostou, E.; Sangid, M. D.; Rollett, A. D. Analyzing the effects of powder and post-processing on porosity and properties of electron beam melted Ti-6Al-4V. *Materials Research Letters* **2017**, *5*, 516–525, Publisher: Taylor & Francis eprint: <https://doi.org/10.1080/21663831.2017.1340911>.
- (50) Ng, G. K. L.; Jarfors, A. E. W.; Bi, G.; Zheng, H. Y. Porosity formation and gas bubble retention in laser metal deposition. *Applied Physics A* **2009**, *97*, 641–649.
- (51) Bellini, C.; Berto, F.; Cocco, V. D.; Iacoviello, F.; Mocanu, L. P.; Razavi, N. Additive manufacturing processes for metals and effects of defects on mechanical strength: a review. *Procedia Structural Integrity* **2021**, *33*, 498–508.
- (52) Cunningham, R. W. Defect Formation Mechanisms in Powder-Bed Metal Additive Manufacturing. Ph.D., Carnegie Mellon University, United States – Pennsylvania, 2018; ISBN: 9780355952520.
- (53) Smith, T. R.; Sugar, J. D.; Schoenung, J. M.; San Marchi, C. Relationship between

- manufacturing defects and fatigue properties of additive manufactured austenitic stainless steel. *Materials Science and Engineering: A* **2019**, *765*, 138268.
- (54) Tang, M.; Pistorius, P. C.; Beuth, J. L. Prediction of lack-of-fusion porosity for powder bed fusion. *Additive Manufacturing* **2017**, *14*, 39–48.
- (55) Pak, P.; Barati Farimani, A. AdditiveLLM: Large language models predict defects in metals additive manufacturing. *Additive Manufacturing Letters* **2025**, *14*, 100292.
- (56) Aboulkhair, N. T.; Maskery, I.; Tuck, C.; Ashcroft, I.; Everitt, N. M. On the formation of AlSi10Mg single tracks and layers in selective laser melting: Microstructure and nano-mechanical properties. *Journal of Materials Processing Technology* **2016**, *230*, 88–98.
- (57) Tang, M.; Pistorius, P. C.; Narra, S.; Beuth, J. L. Rapid Solidification: Selective Laser Melting of AlSi10Mg. *JOM* **2016**, *68*, 960–966.
- (58) Anthropic Anthropic. 2025; <https://www.anthropic.com>.
- (59) modelcontextprotocol/python-sdk. 2025; <https://github.com/modelcontextprotocol/python-sdk>, original-date: 2024-09-24T21:01:35Z.
- (60) Ehtesham, A.; Singh, A.; Gupta, G. K.; Kumar, S. A survey of agent interoperability protocols: Model Context Protocol (MCP), Agent Communication Protocol (ACP), Agent-to-Agent Protocol (A2A), and Agent Network Protocol (ANP). 2025; <http://arxiv.org/abs/2505.02279>, arXiv:2505.02279 [cs].
- (61) Hou, X.; Zhao, Y.; Wang, S.; Wang, H. Model Context Protocol (MCP): Landscape, Security Threats, and Future Research Directions. 2025; <http://arxiv.org/abs/2503.23278>, arXiv:2503.23278 [cs].
- (62) Model context protocol (MCP) - OpenAI Agents SDK. <https://openai.github.io/openai-agents-python/mcp/>.

- (63) Hamsa Buvaraghan; Derek Egan MCP Toolbox for Databases (formerly Gen AI Toolbox for Databases) now supports Model Context Protocol (MCP). 2025; <https://cloud.google.com/blog/products/ai-machine-learning/mcp-toolbox-for-databases-now-supports-model-context-protocol>.
- (64) PyPI The Python Package Index. <https://pypi.org/>.
- (65) Subagents. <https://docs.anthropic.com/en/docs/claude-code/sub-agents>.
- (66) Claude 3.7 Sonnet and Claude Code. <https://www.anthropic.com/news/claude-3-7-sonnet>.
- (67) Introducing Claude 4. <https://www.anthropic.com/news/claude-4>.
- (68) Ghanadi, N.; Son, K.; Alvarado, M.; Yang, S.; Kao, H.-M.; Chang, C.-H.; Paul, B. K.; Pasebani, S. Effect of LPBF Processing Parameters on Inconel 718 Lattice Structures: Geometrical Characteristics, Surface Morphology, and Mechanical Properties. *Materials & Design* **2025**, *253*, 113864.
- (69) Ahmed, N.; Barsoum, I.; Haidemenopoulos, G.; Al-Rub, R. K. A. Process parameter selection and optimization of laser powder bed fusion for 316L stainless steel: A review. *Journal of Manufacturing Processes* **2022**, *75*, 415–434.
- (70) Huang, G.; Chen, H.; Ma, Z.; Zhang, R.; Pei, J.; Lie, Z.; Du, P.; Peng, X.; Liu, Y.; Huang, K. Microstructure and mechanical properties of stainless steel additively manufactured via laser powder bed fusion in high-dense process parameter window. *Materials Science and Engineering: A* **2025**, *928*, 148033.
- (71) Parikh, Y.; Kuttolamadom, M. Property-Graded Stainless Steel 316L by Selective Laser Melting: Characterization & Design. *Journal of Manufacturing Science and Engineering* **2023**, *145*.

- (72) Martendal, C. P.; Esteves, P. D. B.; Lthi, C.; Deillon, L.; Afrasiabi, M.; Bambach, M. Mitigating defects at copper-steel interfaces via a lack of fusion-informed power increment strategy in multi-material laser powder bed fusion. *Materials & Design* **2025**, *258*, 114597.
- (73) Rock, C.; Tarafder, P.; Ives, L.; Horn, T. Characterization of copper & stainless steel interface produced by electron beam powder bed fusion. *Materials & Design* **2021**, *212*, 110278.
- (74) Zhang, S.; Li, Y.; Dai, H.; Zhang, Z.; Chen, X. Achieving balanced uniform and local corrosion performance of SS 316L/IN625 hybrid alloy manufactured by directed energy deposition. *Journal of Materials Research and Technology* **2024**, *32*, 3937–3948.
- (75) Blkba, . S.; Serinda, T.; Grol, U.; Gnen, A.; am, G. Improving oxidation resistance of wire arc additive manufactured Inconel 625 Ni-based superalloy by pack aluminizing. *CIRP Journal of Manufacturing Science and Technology* **2023**, *46*, 89–97.
- (76) Fan, J.-k.; Yang, H.-c.; Zhang, P.-z.; Li, J.-y.; Jing, Z.-j.; Chen, F.-l.; Liu, D.-g.; Tang, B.; Kou, H.-c.; Li, J.-s. Mechanism of high temperature oxidation of Inconel 625 superalloy with various solution and ageing heat treatment processes. *Transactions of Nonferrous Metals Society of China* **2024**, *34*, 3662–3676.
- (77) Gonzalez, J. A.; Mireles, J.; Stafford, S. W.; Perez, M. A.; Terrazas, C. A.; Wicker, R. B. Characterization of Inconel 625 fabricated using powder-bed-based additive manufacturing technologies. *Journal of Materials Processing Technology* **2019**, *264*, 200–210.